Supplement of: All aboard! Earth system investigations with the CH2O-CHOO TRAIN v1.0

Tyler Kukla[1], Daniel E. Ibarra[2,3], Kimberly V. Lau[4], and Jeremy K.C. Rugenstein[1,5]

[1]Department of Geosciences, Colorado State University, Fort Collins, CO, USA
[2]Department of Earth, Environmental and Planetary Sciences, Brown University, Providence, RI, USA
[3]Institute at Brown for Environment and Society, Brown University, Providence, RI, USA
[4]Department of Geosciences and Earth and Environmental Systems Institute, The Pennsylvania State University, University Park, PA, USA
[5]Max Planck Institute for Meteorology, Hamburg, Germany

Correspondence: Jeremy K.C. Rugenstein (Jeremy.Rugenstein@colostate.edu); Tyler Kukla (tykukla@colostate.edu)

1 Introduction

This supplementary materials document includes further information about the Moist Energy Balance Model, details associated with model stability, a more detailed explanation for the overturning direction of the weathering feedback (see text) and tables with default values and citations for model parameters.

2 Moist Energy Balance Model

2.1 Details on the Hadley cell parameterization and calculating latent heat flux divergence

Following Siler et al. (2018), we assign a weighting function to partition between Hadley cell (equatorward) and eddy (poleward) latent heat fluxes where the weight (w) is defined as:

$$w = 1 - \mathrm{e}^{\left(-x^2/0.3^2\right)}. \tag{1}$$

Next, the moist static energy flux of the Hadley cell (in W) is calculated as a fraction of the total poleward flux (F) using the weighting function where:

$$F_{\mathrm{HC}} = (1 - w)F. \tag{2}$$

We then calculate the total equatorward mass transport of the Hadley cell's lower branch (ψ, in kgs^{-1}) from F_{HC} by:

$$\psi = \frac{F_{\mathrm{HC}}}{h_{\mathrm{eq}} - h(x) + g} \tag{3}$$

where h_{eq} is the moist static energy at the equator, $h(x)$ is the zonal pattern of moist static energy, and g is an additional term accounting for gross moist stability that is set to $1.5x10^4$. Finally, ψ is used to calculate $F_{\text{HC,q}}$ following the main text.

2.2 Details on the partitioning of *P* and *E*

To re-iterate from the main text, the equation we use to calculate evaporation (E) is Siler et al. (2019)

$$E = \frac{R_G\alpha + \rho_{\text{air}}c_p(1-rh)C_H u}{\alpha + \frac{c_p}{L_v/q}}. \tag{4}$$

Here, we walk through the parameter values and equations that contribute to this formulation. First, R_G, with units Wm^{-2}, is shorthand for the difference between the surface net downward radiative flux (R_s in Siler et al. (2019)) and the spatial pattern of ocean heat uptake plus heat uptake by frozen hydrometeors at the surface (G in Siler et al. (2019)). We employ an idealized latitudinal profile for this difference where:

$$R_G = R_s - G = 180\left[\left(1-x^2\right) - 0.4\mathrm{e}^{-(x/0.15)^2}\right]. \tag{5}$$

The next term, α, scales the saturation specific humidity (q^*) to its change with temperature (T) such that

$$\frac{dq^*}{dT} = \alpha q^* \tag{6}$$

where

$$\alpha = \frac{L_v}{R_v T^2} \tag{7}$$

with R_v being the specific gas constant for water vapor. Relative humidity (rh) is set to the global constant value of 80% (Hwang and Frierson, 2010; Siler et al., 2018), although other values or latiduinal spatial profiles of rh could be easily defined. C_h is a non-dimensional drag coefficient set to 1.5×10^{-3}. Finally, u is an idealized spatial profile of the surface wind speed (ms^{-1}) defined as:

$$u = 4 + 4\left|sin\left(\frac{\pi x}{1.5}\right)\right|. \tag{8}$$

The idealized formulations for R_G and u are held constant for all climate states in this paper, although it would also be reasonable to allow these functions to vary with climate and geography.

2.3 Model stability

The equations underlying the MEBM are sensitive to the initial conditions in such a way that certain sets of initial conditions can lead to unexpected results that differ substantially from results that represent very small changes to those initial conditions. For example, figure S1A shows how the MEBM climate state varies with the temperature boundary conditions. When the temperature guesses for both poles are warm (up and to the right), the model produces an ice-free solution (yellow region) and when both guesses are sufficiently cold the model generates a fully-glaciated "Snowball" solution (gray polygon). Similar stability maps emerge for other levels of atmospheric CO_2. As CO_2 decreases sufficiently the multiple stable states collapse and the both poles (green) solution space expands. We note that this map corresponds to the meridionally-symmetric "Cat-eye" geography, and other geographic configurations will have different maps influenced by a number of factors, including how symmetric the underlying land and ocean distributions that influence albedo are.

Some pixels in figure S1A are empty, indicating that the model was unable to find a stable solution within ten seconds. This is an arbitrary upper-limit imposed to increase computational efficiency and this limit can be modified by the user. We have found that if a solution is not reached within ten seconds on a laptop PC it is likely that no solution will be reached and the model will time-out after minutes of searching for a solution. The ten-second upper-bound avoids the MEBM stalling in these minutes-long null results.

If the model is not solved in ten seconds or it returns a "snowball" solution, a simple set of rules are followed to identify a nearby, acceptable solution (the user may also update these rules). Specifically, we search for a new, viable boundary condition that can be solved in under ten seconds and does not produce a fully-glaciated result. Figure S1B shows an example of such a search. First, the model searches two steps toward a higher N pole temperature guess (marked by arrow 1), then two steps toward a higher S pole temperature guess (arrow 2), then indefinite steps with higher N pole temperature guesses until a solution is found. Step distance is user-defined (in degrees Celsius). The search stops when the first solution is found. The decision to search indefinitely along the N pole temperature axis rather than along the S pole temperature axis is arbitrary but selected to maintain a simple, reproducible result. We do not move diagonally across the solution space map to minimize the likelihood of moving to an ice-free temperature state when the original temperature guesses are proximal to glaciated solutions.

3 Toy weathering model and $F_{w,sil}$ overturning behavior

Warmer temperatures and more runoff tend to increase weathering fluxes, so when temperature increases while runoff decreases, which effect wins out? Here, we build a toy model to predict whether the silicate weathering feedback is negative (weathering increases with warming due to warmer temperatures) or positive (weathering decreases with warming due to less runoff) based on scaling relationships linking silicate-derived bicarbonate concentrations ($[C]_{sil}$) and runoff (q) to temperature.

To begin, we assume that $[C]$ and q vary linearly with temperature such that

$$[C]_{sil} = m_C T + b_C \tag{9}$$

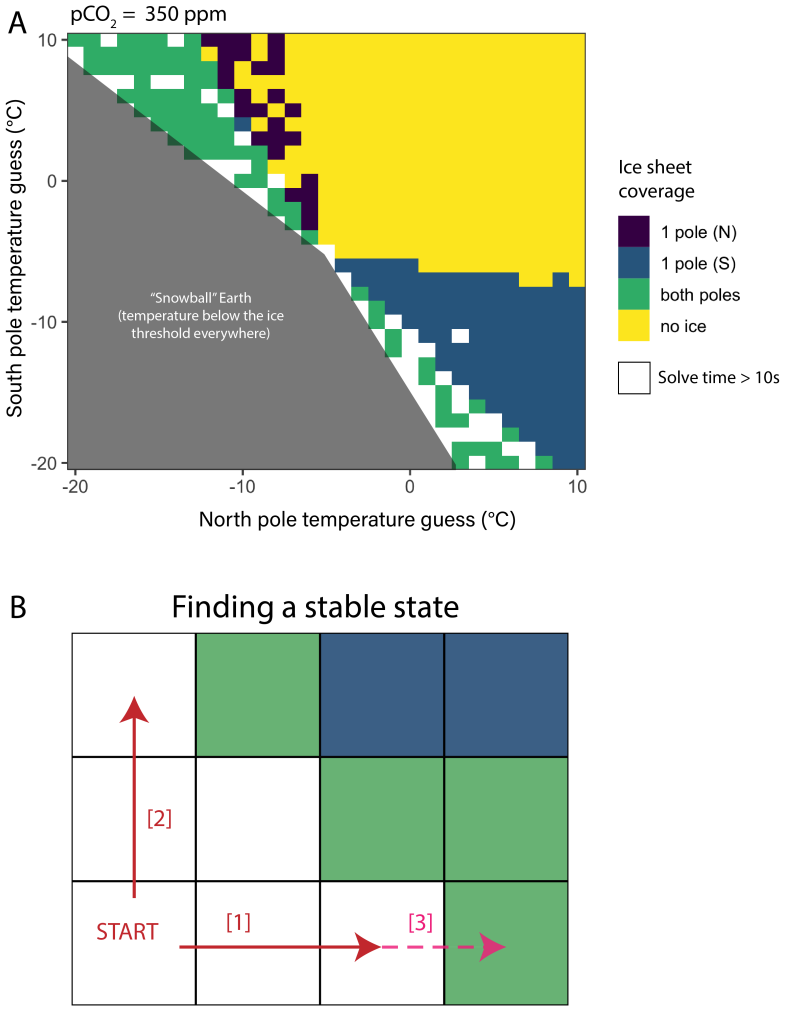

Figure S 1. (**A**) Map of climate state (colors) at different temperature guesses (axes) for atmospheric pCO_2 of 350 ppmv. Warm south and north pole boundary condition temperature guesses give an ice-free solution (yellow), blue and purple represent one glaciated pole, and green is both poles. The gray area to the bottom-left is a "snowball" solution which we deem unreasonable for this work. Blank pixels are where the model took more than 10 seconds to solve. (**B**) If the model takes longer than 10s to solve or returns a snowball, it looks for an acceptable solution following path [1], then [2], then [3] indefinitely until a solution is reached.

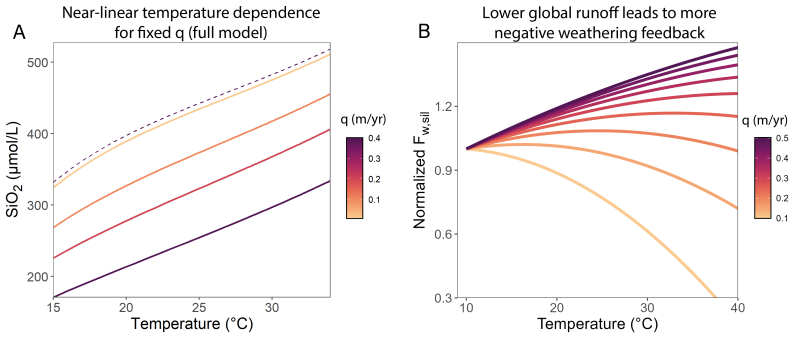

Figure S 2. (**A**) For a fixed runoff value, SiO_2 concentrations increase mostly linearly with global temperature. Dashed line is the theoretical maximum equilibrium concentration. (**B**) Toy model shows that the slope of the weathering response to temperature changes with the initial value of global mean runoff. When the initial global mean runoff is lower, the weathering feedback is more likely to be positive (less weathering with warming) as the effect of temperature on solute concentrations is diminished. The Business belt world simulations effectively move from a higher initial q (darker colored line) in the decreasing ω experiment, to a lower initial q in the increasing ω experiment, flipping the sign of the weathering feedback.

and

$$q = m_q T + b_q \tag{10}$$

where T is temperature and m and b are the slope and intercept terms. Subscripts C and q denote the slope and intercept of the concentration or runoff equations, respectively.

Such linear approximations for $[C]$ and q are supported by the MEBM and weathering model results showing an approximately linear relationship between silicate concentrations and temperature (see Fig. S2A and main text Fig. **??**A). We then write the silicate weathering flux as the product of $[C]_{\text{sil}}$ and q, ignoring a coefficient that would account for converting global runoff to units of discharge for simplicity, and plug in equations 9 and 10 to get the silicate weathering flux $F_{\text{w,sil}}$

$$F_{\text{w,sil}} = (m_C T + b_C)(m_q T + b_q). \tag{11}$$

This model produces the overturning behavior found in the CH2O-CHOO TRAIN (Fig. S2B). When initial runoff values are higher, the effect of temperature on weathering rates is greater, and weathering increases with warming. When runoff is lower, the temperature effect is smaller and weathering decreases with warming. At some intermediate values of initial runoff, the direction of the silicate weathering feedback depends on temperature. We note that the line colors in Fig. S2B denote the value of initial global mean runoff (temperature = 10°C). Runoff changes with temperature following a defined slope based on the Business belt world results.

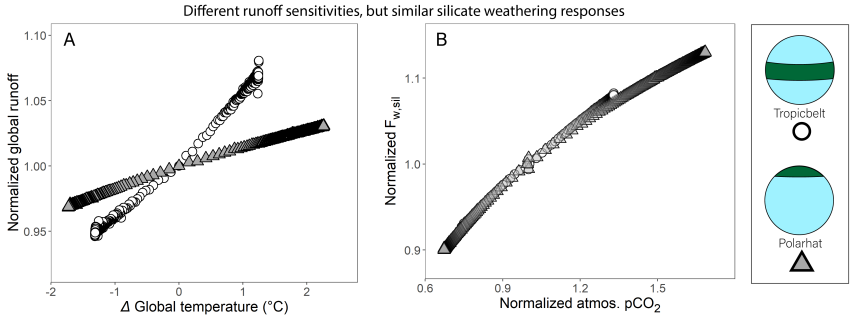

Figure S 3. (**A**) Sensitivity of global runoff to temperature. Runoff is more sensitive to climate in Tropicbelt than Polarhat world. (**B**) Normalized silicate weathering flux response to pCO_2. Despite a weaker runoff sensitivity, Polarhat weathering response is similar to Tropicbelt world due to polar amplification of warming which compensates for the weaker runoff response.

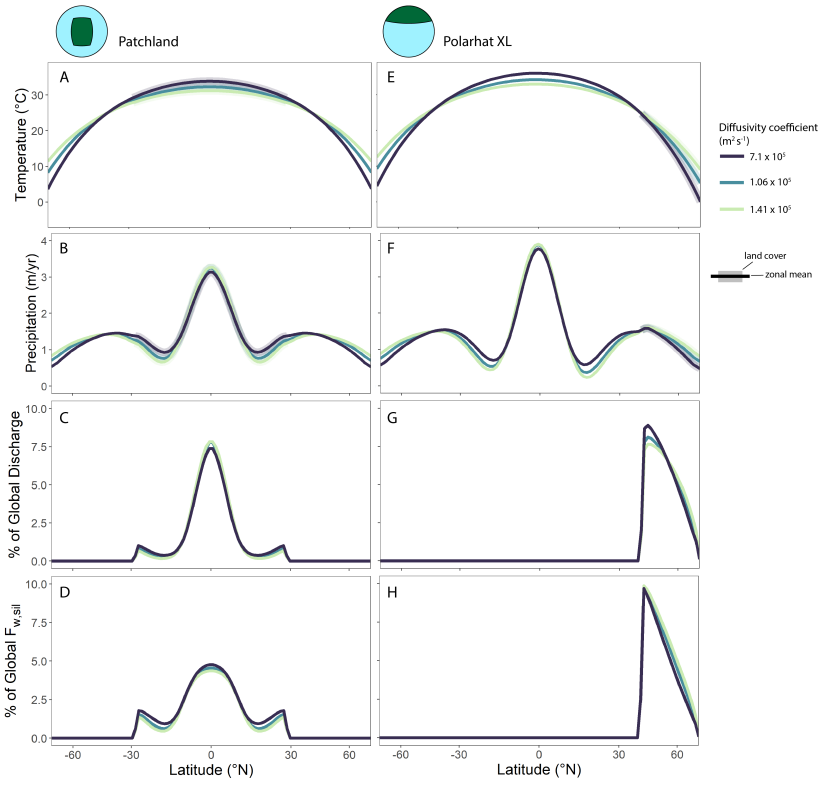

Figure S 4. Zonal mean climate and weathering in Patchland and Polarhat XL. Global temperature **(A, E)**, zonal mean precipitation **(B, F)**, the percent of global discharge **(C, G)**, and the percent of global silicate weathering **(D, H)** for Patchland world (A-D) and Polarhat XL (E-H). Thick, faded line segments in temperature and precipitation panels denote the latitudinal extent of land (whereas discharge and silicate weathering are terrestrial only). Note the trade-off in tropical vs subtropical discharge in Patchland world, leading to temperature-driven changes in weathering driving the climate response.

Table S 1. Input parameters and formulas for MEBM component of model.

Long name	Variable	Value or eq'n	units	See equation(s)	Notes	Reference(s)
Earth's radius	a	6.37×10^6	m	1		
Specific heat of air (constant pressure)	c_p	1004	$J\ kg^{-1}$	2, 6		
Latent heat of vaporization	L_v	2.45×10^6	$J\ kg^{-1}$	2, 5	no temperature dependence	
Surface atmospheric pressure	p_s	1.013×10^5	Pa	3, 4		
Diffusivity coefficient	D	1.06×10^6	$m^2\ sec^{-1}$	3, 4	multiply by $\frac{\rho_a}{g}$ to get kinematic diffusivity	Hwang and Frierson, 2010; Siler et al. 2018
Specific gas constant for vapor	R_v	461	$J\ kg^{-1}$	S7		
Clausius-Clapeyron scaling factor	α	$\frac{L_v}{R_v T^2}$		6		
Near-surface air density	ρ_{air}	1.2	$kg\ m^{-3}$	6		
Relative humidity	rh	0.8		6	bounded [0-1]; global constant	
Bulk transfer coefficient	C_H	1.5×10^{-3}		6		Siler et al. 2019
Near surface wind speed	u	$4 + 4\left\lvert sin\left(\frac{\pi x}{1.5}\right)\right\rvert$	$m\ s^{-1}$	6	idealized zonal mean profile	Siler, pers. comm.
Moisture recycling efficiency	ω	2.6		7	Global mean value	Fu, 1981; Zhang et al. 2004; Greve, 2015
OLR constant (A) intercept	C_{LW}	222.5		10	Often 207 but tuned to higher value for our geographies	Myhre et al. 1998; North and Kim, 2017
OLR constant (A) slope	M	18		10	Often 5.35 but tuned higher for greater clim sensitity	
Water vapor feedback coefficient	B	3.35		9	Blackbody limit is 4.61	North, 1981; North and Kim, 2017; Koll and Cronin, 2018
Ocean albedo	α_{ocean}	0.13			Tunable	
Land albedo	α_{land}	0.2			Tunable	
Ice albedo	α_{ice}	0.75			Tunable; higher values = stronger ice albedo feedback	
Ice formation threshold	T_{ice}	-5	$^\circ C$			

Table S 2. Input parameters and formulas for weathering component of model.

Long name	Variable	Value or eq'n	units	See equation(s)	Notes	Reference(s)
Reactive length scale × eff. porosity	$L\phi$	0.1		12		Maher and Chamberlain, 2014
Theoretical max reaction rate	r_{max}	1085	$\mu mol\ SiO_2\ L^{-1}\ y^{-1}$	12		Maher and Chamberlain, 2014
Activation energy	Ea	38	$kJ\ mol$	13		Maher and Chamberlain, 2014
Init. max equilibrium silicate-derived carbonate	$[C]_{\text{sil,eq,0}}$	374	$\mu mol\ L^{-1}$	14		Maher and Chamberlain, 2014
Reference reaction rate	k_{reac}	8.7×10^{-6}	$mol\ m^{-2}\ y^{-1}$	13		Maher and Chamberlain, 2014
Soil age	T_s	2000	yr	12		Maher and Chamberlain, 2014
Max GPP	GPP_{max}	$2 \times GPP_0$		16	GPP_0 is set to one	Volk, 1989
Minimum pCO_2	$pCO_{2,\text{min}}$	100	ppmv	17		Volk, 1989; Prentice and Harrison, 2009; Scheff et al. 2017
Land area	A_{land}	variable	m^2	18	Calculated from input geography file	

Table S 3. Input parameters and formulas for weathering component of model.

Long name	Variable	Value or eq'n	units	See equation(s)	Notes	Reference(s)
Initial DIC carbon isotope composition	$\delta^{13}C_i$	0	‰	20		
Volcanism carbon isotope composition	$\delta^{13}C_{\text{volc}}$	-5	‰	20		Kump and Arthur (1999)
Carbonate weathering carbon isotope composition	$\delta^{13}C_{\text{w,carb}}$	0	‰	20		Kump and Arthur (1999)
Inorganic carbon minus organic carbon isotope composition	ϵ	27	‰	20		Kump and Arthur (1999)
Mean ocean temperature	T_o	$T_a - 10$	$^\circ C$	T_a is global mean air temperature		Key et al. (2004)
Ocean salinity	(not shown)	35	PSU			Key et al. (2004)
Mean ocean pressure	(not shown)	300	bar		Approximation	
Seawater Ca concentration	[Ca]	15	$mol\ L^{-1}$		Approx. Phanerozoic mean	Lowenstein et al. (2001); Brennan et al. (2013); Horita et al. (2002); Timofeeff et al. (2006)
Seawater Mg concentration	[Mg]	48.5	$mol\ L^{-1}$		Approx. Phanerozoic mean	Lowenstein et al. (2001); Brennan et al. (2013); Horita et al. (2002); Timofeeff et al. (2006)
Seawater sulfate concentration	[SO4]	28.2	$mol\ L^{-1}$			Broecker and Peng (1982)
Ocean water volume	(not shown)	1.4×10^{21}	L			Caves Rugenstein et al. (2019)
Initial ocean pH	pH_i	8.2				Hönisch et al. (2009)
Initial volcanic flux	F_{volc}	8×10^{12}	$mol\ yr^{-1}$	19, 20, 22, 23		Caves Rugenstein et al. (2019)
Initial carbonate weathering flux	$F_{\text{w,carb}}$	12×10^{12}	$mol\ yr^{-1}$	19, 20, 21, 23		Caves Rugenstein et al. (2019)
Initial carbonate burial flux	$F_{\text{b,carb}}$	20×10^{12}	$mol\ yr^{-1}$	19, 20, 21		Caves Rugenstein et al. (2019)
Initial organic carbon weathering flux	$F_{\text{w,org}}$	8×10^{12}	$mol\ yr^{-1}$	19, 20		Caves Rugenstein et al. (2019)
Initial organic carbon burial flux	$F_{\text{b,org}}$	8×10^{12}	$mol\ yr^{-1}$	19, 20		Caves Rugenstein et al. (2019)

References

Brennan, S. T., Lowenstein, T. K., and Cendon, D. I.: The Major-Ion Composition of Cenozoic Seawater: The Past 36 Million Years from Fluid Inclusions in Marine Halite, American Journal of Science, 313, 713–775, https://doi.org/10.2475/08.2013.01, 2013.

Broecker, W. S. and Peng, T. H.: Tracers in the Sea, vol. 24, Eldigio Press, Palisades, N.Y., third edn., 1982.

Caves Rugenstein, J. K., Ibarra, D. E., and von Blanckenburg, F.: Neogene Cooling Driven by Land Surface Reactivity Rather than Increased Weathering Fluxes, Nature, 571, 99–102, https://doi.org/10.1038/s41586-019-1332-y, 2019.

Hönisch, B., Hemming, N. G., Archer, D., Siddall, M., and McManus, J. F.: Atmospheric Carbon Dioxide Concentration Across the Mid-Pleistocene Transition, Science, 324, 1551–1554, https://doi.org/10.1126/science.1171477, 2009.

Horita, J., Zimmermann, H., and Holland, H. D.: Chemical Evolution of Seawater during the Phanerozoic: Implications from the Record of Marine Evaporites, Geochimica et Cosmochimica Acta, 66, 3733–3756, 2002.

Hwang, Y. T. and Frierson, D. M.: Increasing Atmospheric Poleward Energy Transport with Global Warming, Geophysical Research Letters, 37, 1–5, https://doi.org/10.1029/2010GL045440, 2010.

Key, R. M., Kozyr, A., Sabine, C. L., Lee, K., Wanninkhof, R., Bullister, J. L., Feely, R. A., Millero, F. J., Mordy, C., and Peng, T.-H.: A Global Ocean Carbon Climatology: Results from Global Data Analysis Project (GLODAP): GLOBAL OCEAN CARBON CLIMATOLOGY, Global Biogeochemical Cycles, 18, n/a–n/a, https://doi.org/10.1029/2004GB002247, 2004.

Kump, L. R. and Arthur, M. A.: Interpreting Carbon-Isotope Excursions: Carbonates and Organic Matter, Chemical Geology, 161, 181–198, https://doi.org/10.1016/S0009-2541(99)00086-8, 1999.

Lowenstein, T. K., Timofeeff, M. N., Brennan, S. T., Hardie, L. A., and Demicco, R. V.: Oscillations in Phanerozoic Seawater Chemistry: Evidence from Fluid Inclusions, Science, 294, 1086–1088, https://doi.org/10.1126/science.1064280, 2001.

Siler, N., Roe, G. H., and Armour, K. C.: Insights into the Zonal-Mean Response of the Hydrologic Cycle to Global Warming from a Diffusive Energy Balance Model, Journal of Climate, 31, 7481–7493, https://doi.org/10.1175/JCLI-D-18-0081.1, 2018.

Siler, N., Roe, G. H., Armour, K. C., and Feldl, N.: Revisiting the Surface-Energy-Flux Perspective on the Sensitivity of Global Precipitation to Climate Change, Climate Dynamics, 52, 3983–3995, https://doi.org/10.1007/s00382-018-4359-0, 2019.

Timofeeff, M. N., Lowenstein, T. K., da Silva, M. A. M., and Harris, N. B.: Secular Variation in the Major-Ion Chemistry of Seawater: Evidence from Fluid Inclusions in Cretaceous Halites, Geochimica et Cosmochimica Acta, 70, 1977–1994, https://doi.org/10.1016/j.gca.2006.01.020, 2006.